# Atomic Structure Evolution of Pt-Co Binary Catalysts: Single Metal Sites versus Intermetallic Nanocrystals

X. Li, L. Ma

# DISCLAIMER

# Atomic Structure Evolution of Pt–Co Binary Catalysts: Single Metal Sites versus Intermetallic Nanocrystals

*Xing Li, Yanghua He, Shaobo Cheng, Boyang Li, Yachao Zeng, Zhenhua Xie, Qingping Meng, Lu Ma, Kim Kisslinger, Xiao Tong, Sooyeon Hwang, Siyu Yao, Chenzhao Li, Zhi Qiao, Chongxin Shan, Yimei Zhu, Jian Xie, Guofeng Wang,\* Gang Wu,\* and Dong Su\**

Due to their exceptional catalytic properties for the oxygen reduction reaction (ORR) and other crucial electrochemical reactions, PtCo intermetallic nanoparticle (NP) and single atomic (SA) Pt metal site catalysts have received considerable attention. However, their formation mechanisms at the atomic level during high-temperature annealing processes remain elusive. Here, the thermally driven structure evolution of Pt–Co binary catalyst systems is investigated using advanced in situ electron microscopy, including PtCo intermetallic alloys and single Pt/Co metal sites. The pre-doping of $CoN_4$ sites in carbon supports and the initial Pt NP sizes play essential roles in forming either $Pt_3Co$ intermetallics or single Pt/Co metal sites. Importantly, the initial Pt NP loadings against the carbon support are critical to whether alloying to $L1_2$-ordered $Pt_3Co$ NPs or atomizing to SA Pt sites at high temperatures. High Pt NP loadings (e.g., 20%) tend to lead to the formation of highly ordered $Pt_3Co$ intermetallic NPs with excellent activity and enhanced stability toward the ORR. In contrast, at a relatively low Pt loading (<6 wt%), the formation of single Pt sites in the form of $PtC_3N$ is thermodynamically favorable, in which a synergy between the $PtC_3N$ and the $CoN_4$ sites could enhance the catalytic activity for the ORR, but showing insufficient stability.

## 1. Introduction

Developing cost-effective yet durable electrocatalysts for the oxygen reduction reaction (ORR) is a significant challenge for proton-exchange-membrane fuel cells (PEMFCs). PtM-based alloy nanoparticles (NPs) with optimized morphology and structure have presented significantly improved ORR catalytic activity.[1–4] Among studied Pt-based catalysts, PtCo intermetallic catalysts, especially the $L1_0$- or $L1_2$-ordered PtCo alloys, have been considered as one of the most promising candidates due to their optimized binding energy with oxygen and promising catalytic stability during the ORR.[3,5,6] On the other hand, single atomic (SA) Pt site catalysts on nitrogen (N)-doped carbon support is a new class of catalysts and have exhibited unique electrochemical properties for many crucial electrochemical reactions

X. Li, C. Shan
Henan Key Laboratory of Diamond Optoelectronic Materials
and Devices
Key Laboratory of Material Physics
Ministry of Education
School of Physics and Microelectronics
Zhengzhou University
Zhengzhou 450052, China
X. Li, K. Kisslinger, X. Tong, S. Hwang, D. Su
Center for Functional Nanomaterials
Brookhaven National Laboratory
Upton, NY 11973, USA
E-mail: dongsu@iphy.ac.cn
X. Li, S. Cheng, Q. Meng, Y. Zhu
Condensed Matter Physics and Materials Science
Brookhaven National Laboratory
Upton, NY 11973, USA
Y. He, Y. Zeng, Z. Qiao, G. Wu
Department of Chemical and Biological Engineering
University at Buffalo
The State University of New York
Buffalo, NY 14260, USA
E-mail: gangwu@buffalo.edu

B. Li, G. Wang
Department of Mechanical Engineering and Materials Science
University of Pittsburgh
Pittsburgh, PA 15261, USA
E-mail: guw8@pitt.edu
Z. Xie, S. Yao
Chemistry Division
Brookhaven National Laboratory
Upton, NY 11973, USA
L. Ma
National Synchrotron Light Source II
Brookhaven National Laboratory
Upton, NY 11973, USA
C. Li, J. Xie
Department of Mechanical Engineering
Purdue School of Engineering and Technology
Indiana University-Purdue University
Indianapolis, IN 46202, USA
D. Su
Beijing National Laboratory for Condensed Matter Physics
Institute of Physics
Chinese Academy of Sciences
Beijing 100190, China

capable of significantly reducing Pt loadings.[7–11] Both types of catalysts are often synthesized by controlling a thermal activation process on porous carbon supports.[12–17] In particular, zeolitic-imidazolate-framework-8 (ZIF-8)-derived carbon supports (denoted as NC) can provide coordinatively unsaturated sites and defects to anchor PtCo NPs or single metal sites. The porous NC also can stimulate the fast adsorption of reactants and desorption of products during the synthesis.[1,10,14,18–23] However, the formation of ordered intermetallic NPs and SA sites stemmed from pre-deposited Pt NPs on the NC support are complicated physical and chemical processes,[2,14,16,24–26] which are hard to control their ordered structures and atomic dispersion accurately. Therefore, elucidating the influence of synthetic conditions on the structural evolution of both types of Pt-based catalysts can provide an understanding for the rational design to achieve desired catalytic properties.[27–31]

During the synthesis, the thermal treatment is critical to governing the morphology, composition, and structure of PtCo alloys and their interactions with the single metal site rich NC support (e.g., $FeN_4$ or $CoN_4$).[9,12,32–37] Recently, we found that the Pt NPs deposited on the single Co atomic sites ($CoN_4$)-rich NC can be transformed to highly ordered $Pt_3Co$ NPs during the controlled thermal activation process.[1] The disorder–order transition in PtCo NPs with well-controlled stoichiometry has been studied.[30,38] However, the interaction between Pt NPs and single metal $CoN_4$ sites embedded in carbon remains unclear during the alloying or atomization processes.[29,39–43] An understanding of the structural evolution of Pt NPs at the atomic level still lacks. Especially, key factors influencing the competition between atomization and alloying process remain elusive. It is desirable to develop a real-time atomic resolution microscopic approach to dynamically tracking the kinetic reaction process and elucidating their formation mechanisms.[44–50]

Here, we present a direct observation of the composition and structure evolution of Pt NPs on atomically dispersed $CoN_4$-site-rich NC supports (PtCo/NC) during high-temperature annealing with in situ transmission electron microscopy (TEM) techniques. We discovered that individual alloying or atomization evolutions of Pt NPs depend on the initial Pt loadings against the NC support, leading to the formation of ordered PtCo intermetallics and Pt/Co single metal site catalysts, respectively. Both Pt–Co catalysts show promising catalytic activity for the ORR. In particular, theoretical calculations and in-depth experimental characterization reveal a synergy between single Pt and Co sites embedded in carbon support, enhancing their overall ORR activity. However, such single Pt sites are not stable for the ORR under dynamic potentials, while the ordered $Pt_3Co$ intermetallic NPs exhibited enhanced stability. This study provided an insight into the formation mechanism, structure evolution, and catalytic activity and stability for these two types of Pt–Co catalysts (e.g., ordered intermetallic alloys versus single Pt sites), which establishes the crucial synthesis–structure–property correlation.

## 2. Results and Discussion

### 2.1. Pt-Loading-Dependent Structural Evolution

The atomically dispersed $CoN_4$ site rich NC support derived from ZIF-8 (Co/NC) was employed for dispersing Pt NPs with different Pt mass loadings against the support ($n$PtCo/NC, $n$ represents the mass loading of Pt, $n$ =20, 6, or 1 wt%). The synthesis process is illustrated in **Figure 1**a (see the Experimental Section). High-angle annular dark-field scanning transmission electron microscopy (HAADF-STEM) images
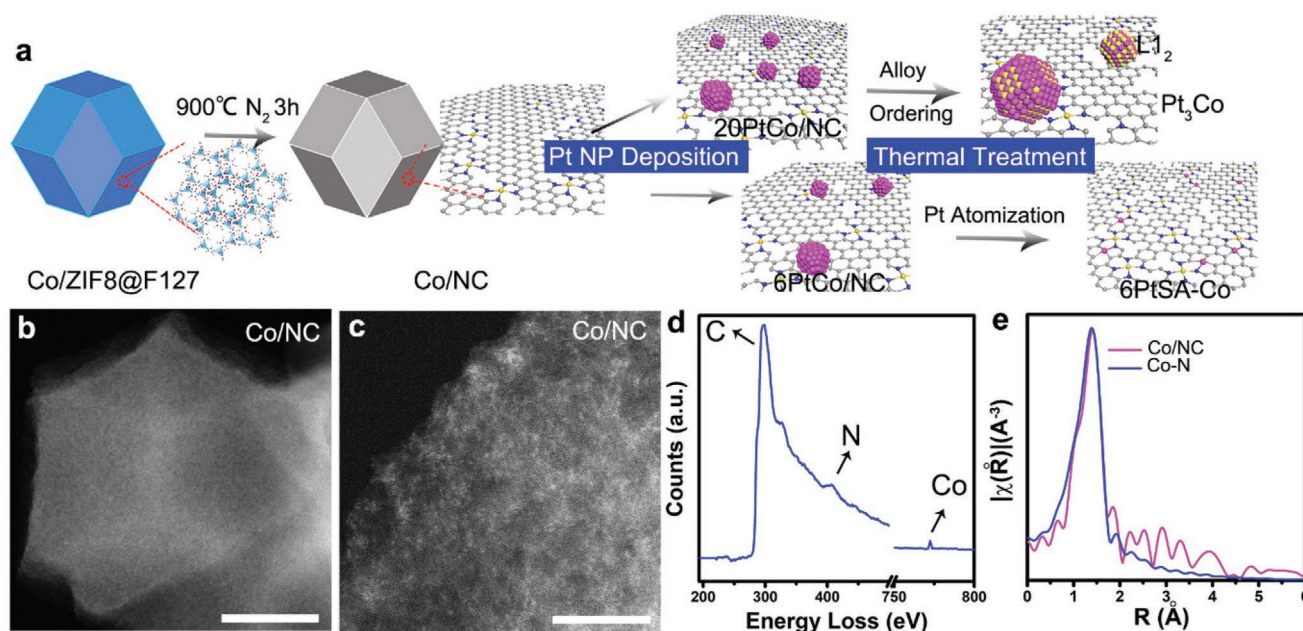


**Figure 1.** Synthesis procedure and characterization of the Co/NC support. a) Schematics showing the synthesis process of $n$PtCo/NC. b) Low- (scale bar: 50 nm) and c) high-magnification STEM images (scale bar: 5 nm) of the Co/NC. d) EELS spectrum and e) the Fourier transform of the $k^3$-weighted EXAFS (data-pink, fit-blue) of the Co/NC.
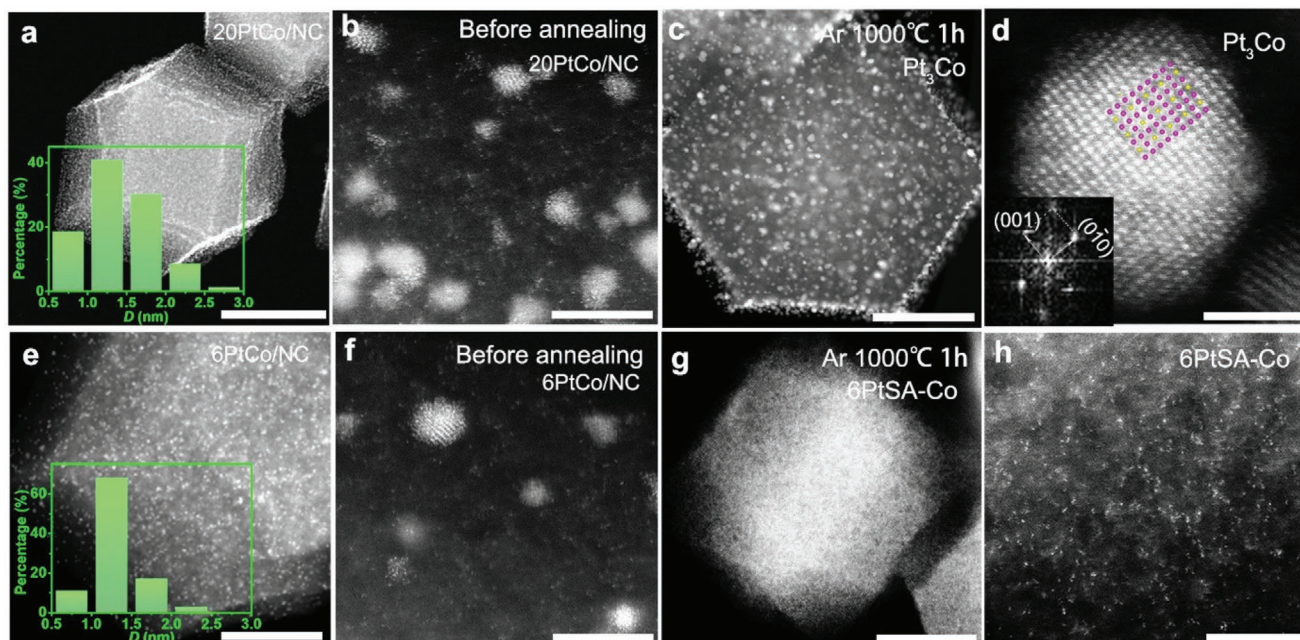
**Figure 2.** Characterization of the 20PtCo/NC and the 6PtCo/NC catalysts before and after annealing, respectively. a) Low- (scale bar: 200 nm) and b) high-magnification STEM images of the 20PtCo/NC (scale bar: 5 nm). Inset in (a) shows the size distribution of Pt NPs. c) Low- (scale bar: 100 nm) and d) high-magnification STEM images of the $Pt_3Co$ NP (scale bar: 2 nm). Corresponding FFT pattern and the atomic structure of $Pt_3Co$ are shown on the lower-left corner and the upper right corner of (d), respectively. e) Low- (scale bar: 50 nm) and f) high-magnification STEM images of 6PtCo/NC (scale bar: 5 nm). Inset in (e) shows the size distribution of Pt NPs. g) Low- (scale bar: 50 nm) and h) high-magnification STEM images of the 6PtSA-Co (scale bar: 5 nm).

in Figure 1b,c show that the individual Co sites uniformly disperse in the NC support. The co-existence of C, N, and Co at the atomic level in the Co/NC support was confirmed by the electron energy loss spectrum (EELS) (Figure 1d). As revealed by the $k^3$-weighted extended X-ray absorption fine structure (EXAFS) spectrum at the Co K-edge (Figure 1e), the Co/NC support presents a prominent peak at ≈1.4 Å (phase uncorrected distance) from the Co—N. The relevant fitting results suggest that N ligands coordinates and stabilizes single Co sites, likely in $CoN_4$.[21] After further depositing Pt NPs with different loadings, the 20PtCo/NC and the 6PtCo/NC samples present similar Pt NP sizes: 1.5 ± 0.4 and 1.3 ± 0.3 nm (**Figure 2**a,e, and 2b,f), respectively. Also, the dispersed density of Pt NPs on the 6PtCo/NC sample is lower (Figure S1a–d, Supporting Information). As revealed by our STEM tomography in Supporting Videos S1 and S2, Supporting Information, the Pt NPs were primarily loaded at the surface of the Co/NC.

After an annealing process at 1000 °C under Ar atmosphere, $L1_2$ ordered $Pt_3Co$ NPs and uniformly dispersed Co SAs were found in the annealed 20PtCo/NC sample (denoted as $Pt_3Co$) (Figure 2c,d; Figure S1e, Supporting Information). In contrast, SA Pt and Co sites dominate in the annealed 6PtCo/NC sample (denoted as 6PtSA-Co) (Figure 2g,h). When the Pt loading was further reduced to 1.0 wt%, we also observed dominant single Pt and Co sites in the NC after the annealing treatment (denoted as 1PtSA-Co) (Figure S2, Supporting Information). The loading-dependent structural evolution of Pt NPs on the Co/NC support is discovered for the first time. To elucidate the competition mechanisms between alloying and atomization

at different Pt loadings, the composition, size, and structure evolutions of Pt NPs were further investigated by using in situ TEM techniques.

## 2.2. Elucidating the Kinetic Alloying Process of Pt NPs with Single Co Sites

We studied the alloying process of Pt NPs by monitoring the elemental distribution of Pt and Co at different temperatures using STEM–energy-dispersive X-ray (STEM–EDX) mappings. As shown in **Figure 3**a, when elevating temperatures from RT to 1000 °C, the well-dispersed single Co metal sites in the 20PtCo/NC sample gradually diffused into Pt NPs and formed PtCo alloyed NPs (Figure S3a, Supporting Information). The formation and growth of Co NPs were not observed during this process. According to our EDX mapping results, the quantified Co/Pt atomic ratio in PtCo NPs (Figure 3b) gradually increased to ≈0.3 during annealing up to 1000 °C (Figure S3b and Table S1, Supporting Information), consistent with the $Pt_3Co$ intermetallic stoichiometry.

With in situ HR-STEM imaging (Figure 3c–h), we further revealed the atomic structural evolution of Pt NPs under gradually increasing temperatures. As shown in Figure 3d–f, we observed that single Co sites migrated from the NC support and surrounded the surface of Pt NPs at 400–600 °C. Then, the gathered Co sites around Pt NP (Figure 3f) disappeared at 800 °C (Figure 3g), suggesting the likely diffusion of Co sites into Pt NPs. Along with this process, the particle migration coalescence (PMC) process of PtCo NPs was frequently observed
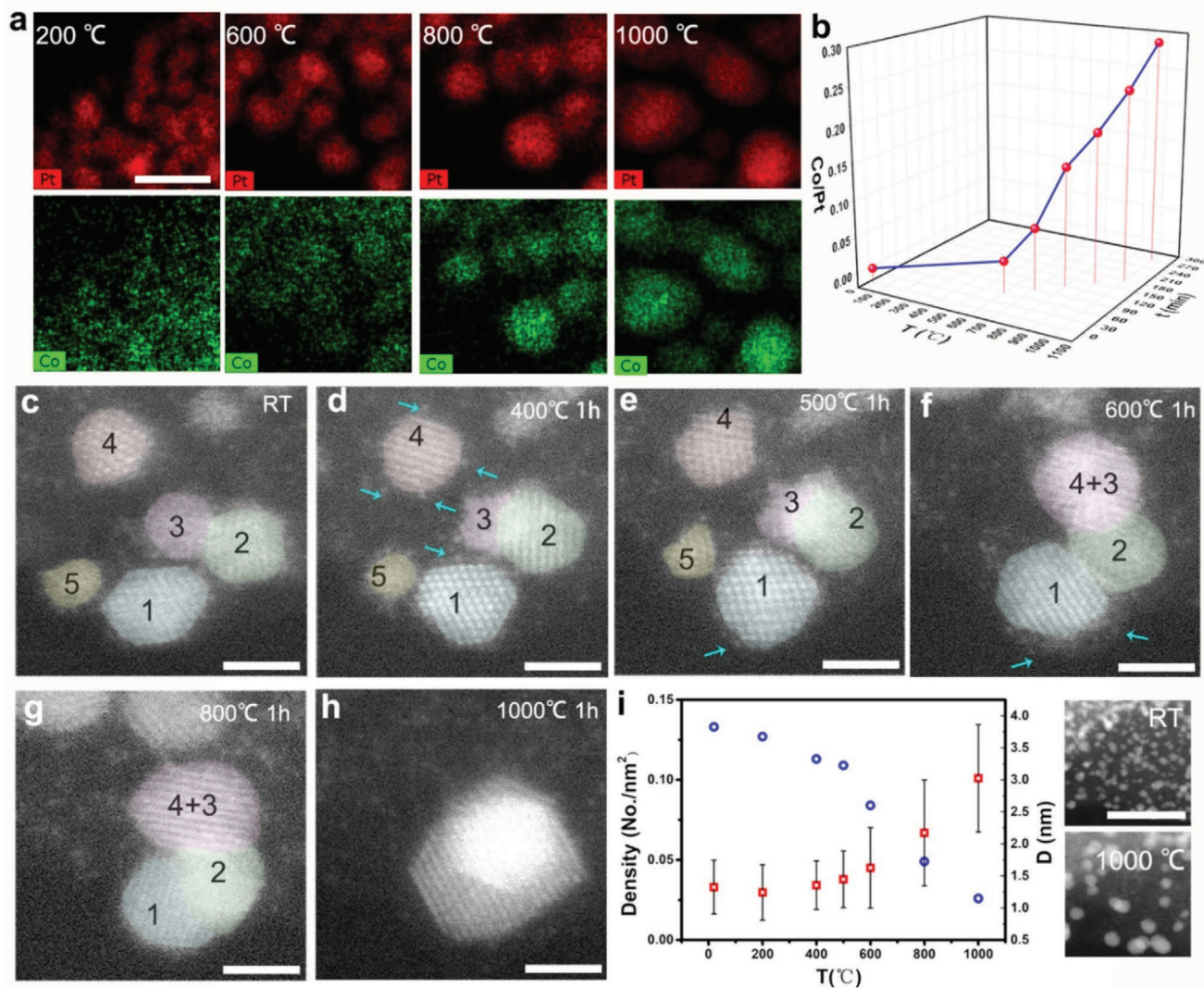
**Figure 3.** Dynamic observation on the alloying process of Pt–Co catalyst during thermal activation. a) EDX mapping of Pt and Co species in the 20PtCo/NC sample after annealing at 200, 600, 800, and 1000 °C (scale bar: 10 nm). b) The atomic ratio between Co and Pt as functions of temperatures ($T$) and time ($t$). c–h) HR-STEM images showing the structure and interaction of Pt NPs with single Co sites after annealed for 1 h at RT (c), 400 °C (d), 500 °C (e), 600 °C (f), 800 °C (g), and 1000 °C (h), respectively (scale bar: 2 nm). i) Particle density and diameter ($D$) as the function of $T$ in a specific region. The STEM images present particle size and density changes in the same region before and after 1000 °C annealing (scale bar: 20 nm).

at 600–1000 °C (Figure 3f–h). The diffusion of single Co sites and the PMC process were accelerated above ≈600 °C and eventually triggered the alloying process, leading to the size increase and density decrease of Pt NPs (Figure 3b,i; Figure S4, Supporting Information). At 1000 °C, the elemental diffusion and disorder–order transformation occur within the alloyed PtCo NP, eventually reaching an atomic ratio of Co to Pt close to ≈0.33 (Figures S5a–c and S6, Supporting Information). The high-temperature annealing provides the activation energy for the diffusion of single Co metal sites into Pt NPs, leading to the uniform distribution of Co in each PtCo alloyed NP. As a comparison, we found that the atomic ratios of Co in PtCo NPs are not uniform if Co NPs, instead of atomic sites, exist on the NC support (Figure S5d,e, Supporting Information). Therefore, the initial Co structures (e.g., NPs or SAs) in the support play a critical role in the final Co distribution within PtCo alloy NPs.

### 2.3. Studying the Atomization Process of Pt NPs

When the initial Pt NP loading on the support is decreased to 6 wt%, we found that the alloying process between Pt NPs and single Co site in the NC support is not favorable at high temperatures. Instead, the Pt NPs tend to be atomized and form single Pt sites uniformly dispersed in the NC support. To understand the formation mechanism, we investigated the in situ atomization process of Pt NPs on the 6PtCo/NC sample. The STEM–EDX mappings showed that the majority of the Pt NPs was gradually disappeared when the annealing temperature was up to 1000 °C (Figure S7, Supporting Information), showing atomically distributed Pt and Co species in the NC support simultaneously (Figure S8, Supporting Information). Through tracking the morphology and size evolution of several Pt NPs in a temperature range of 400–1000 °C (**Figure** 4a–c;
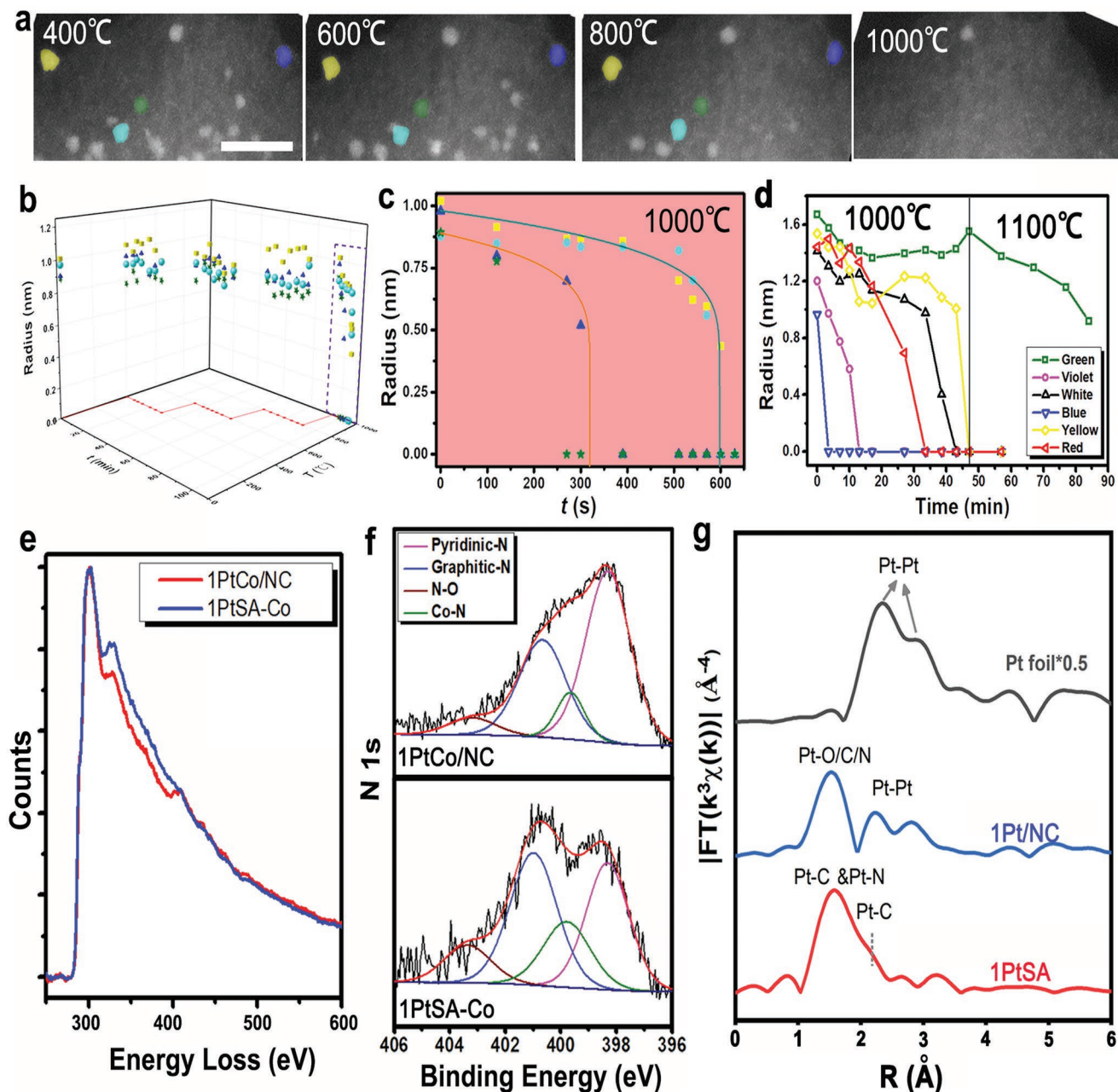
**Figure 4.** Structural evolution of Pt NPs during the atomization process. a) HAADF-STEM images showing the particle size change of the 6PtCo/NC sample with annealing (scale bar: 10 nm). b) The radius evolution of the four colored Pt NPs with $T$ and $t$. The $XY$ projection shows the heating curve. c) The radius evolution of the Pt NPs with t at 1000 °C (points: experimental results; solid line: fitting curves). d) Size changes of Pt NPs with different radius during heating at 1000 and 1100 °C. e) EELS spectra and f) XPS spectra of N1s of the 1PtCo/NC and the 1PtSA-Co. g) The $k^2$-weighted R-space FT spectra from EXAFS for Pt foil*0.5, 1Pt/NC, and 1PtSA.

Figure S9, Supporting Information), we found that the colored Pt NPs (Figure 4a) with the original radius of ≈1 nm gradually were vanished at 1000 °C (Figure S9).

Moreover, the initial size of Pt NPs is critical to the required time duration and temperature for a complete Pt atomization process (Figure 4d; Figure S10, Supporting Information). Smaller Pt NPs require relatively lower temperatures and shorter duration to initiate and complete the atomization process than large ones. For example, the atomization of Pt NPs

with radius of ≈0.5, ≈1, and ≈1.7 nm was found to initiate at 600 (Figure S11a–e, Supporting Information), 1000, and 1100 °C, respectively (Figure 4d). Also, extended time was needed for fully atomizing large Pt NPs even at 1000 °C (Figure 4c,d).

Unlike the reported high-temperature induced atomization behavior of Pt NPs on ZIF-8 crystals,[12] we did not find the apparent thermal motion of Pt NPs within the ZIF-8. Instead, we found that the NC support carbonized from the ZIF-8, regardless of containing single Co sites or not, is necessary for

**ADVANCED
SCIENCE NEWS**

www.advancedsciencenews.com

**ADVANCED
MATERIALS**

www.advmat.de

atomizing Pt NPs (Figure S10, Supporting Information). Thus, the atomization mechanisms can be significantly altered by the nature of supports (e.g., ZIF crystals or ZIF-derived NCs).

An analytical model was adopted to fit the size evolution of Pt NPs, aiming to gain insights into the impacts of size and temperature on atomization kinetics. Due to the relatively high Pt vapor pressure around the ultra-small Pt NPs (Gibbs–Thomson effect) at 1000 °C,[41,47] Pt atoms could escape from Pt NPs and subsequently be captured by the defects in the NC support. Since this process is a surface ripening process, we adopted the model modified by Parker and Campbell (see Supporting Information), which fitted well for Pt NPs with a diameter 6 nm.[51] As presented by the two solid lines in Figure 4c, the two fitting results with different initial radius but identical activation energy ($E_{tot}$) of 400.8 kJ mol$^{-1}$ match well with our experimental radius decay, further confirming that the atomization behavior is associated with the initial size of Pt NPs (Figure S11f, Supporting Information). Since the constant $K_{int}$ with all of the constant prefactors (Equation (S3), Supporting Information) is sensitive to annealing temperatures, our calculations show that $K_{int} = 5.53 \times 10^{-9}$ at 800 °C raises to $6.42 \times 10^{-6}$ at 1000 °C, suggesting that the size reduction rates of the NPs during the atomizing process can be significantly accelerated at higher temperatures (Figure S11g, Supporting Information). Our analysis quantitatively reveals a correlation between the Pt NP size and the annealing temperature in determining the atomization kinetics of Pt NPs supported on the NC.

The bonding nature of single Pt sites on two NC supports with or without CoN$_4$ sites was compared using spectroscopic methods (Figure 4e–g). An ultra-low 1.0 wt% Pt NP loading (e.g., 1PtCo/NC and 1Pt/NC samples) was studied to avoid the influence caused by the nonuniformity of loaded Pt NPs on these NC supports. According to the acquired EELS spectra in Figure 4e, the N-K edge's apparent intensity (≈400 eV) was reduced in the 1PtSA-Co sample (after annealing) compared to the 1PtCo/NC (before annealing). The reduced N content (from 6.18 to 2.61 at%) due to the annealing treatment was also confirmed by the X-ray photoelectron spectroscopy (XPS) (Table S2, Supporting Information). High-resolution XPS spectra further revealed that the reduced N content was mainly pyridinic-N (Figure 4f; Table S3, Supporting Information). Similar phenomena were also observed in the 20PtCo/NC and the 6PtCo/NC samples (Figures S12 and S13, Supporting Information). Therefore, the reduction of N content can be attributed to the unstable N−C bonding in the NC support at high temperatures.[34] Although the sublimation of Zn species in the NC was observed during the annealing process, the content of Pt and Co almost remained the same during the atomization process (Table S2 and Figure S14, Supporting Information).

Furthermore, we employed simple Co-free model samples to study the possible coordination environment of single Pt sites before and after the atomizing process. As revealed by the k$^3$-weighted EXAFS of Pt L3-edge (Figure 4g), the 1Pt/NC sample (before annealing) presents a remarkable peak (≈1.5 Å) originated from the Pt−C/N/O bonding and a pair-peak (≈2.2 and 2.8 Å) associated with the Pt−Pt bonding (referring to the counterparts in Pt foil). The 1000 °C- annealed-1Pt/NC

(i.e., 1PtSA) sample only presents one prominent peak centered around ≈1.5 Å, which likely originated from either Pt−C or Pt−N bonds.[52,53] These results confirmed the complete atomization of Pt clusters on the 1Pt/NC sample during high-temperature annealing, in good agreement with the HR-STEM observations. To quantitatively explore the coordination environment surrounding the central Pt sites in the 1PtSA sample, the Fourier transform of EXAFS fitting (Figure S15, Supporting Information) was carried out with different models (PtC$_4$, PtN$_4$, and PtC$_{4-x}$N$_x$). The most reasonable fitting result (Table S4, Supporting Information) is the PtC$_{4-x}$N$_x$ model, in which a central Pt site is coordinated by two carbon ($CN_{Pt-C} = 3.3 \pm 0.3$, the bond length of 2.03 Å) and one nitrogen ($CN_{Pt-N} = 0.7 \pm 0.5$, the bond length of 2.19 Å), that is, most likely a PtC$_3$N configuration.

### 2.4. Competition between Alloying and Atomization Process

The PMC behaviors of supported NPs greatly depend on their size, support properties, and separation distance.[54–58] Since samples with high and low Pt loadings possess similar NP sizes and the same NC support, the separation distance is considered as the main factor leading to the different behaviors of Pt NPs . The competition between the alloying and the atomization processes in samples with different Pt loadings was elucidated using the first-principles density functional theory (DFT) calculations. Since the average distances between Pt NPs on low (6 wt%) and high (20 wt%) loading samples were ≈3 and ≈1 nm (Figure S1, Supporting Information), respectively. Agglomeration and growth of larger Pt NPs (Figure S16, Supporting Information) with exposed Pt (111) surfaces (Figures S5 and S6, Supporting Information) were observed in the 20PtCo/NC sample during the annealing process due to the small separation distance. In contrast, Pt NPs in the 6PtCo/NC sample remained small diameters (≈1–2 nm) under identical annealing (Figure 4a,b) because of sufficient separation distance among NPs. Herein, an extended Pt (111) surface and a small Pt$_{55}$ cluster with a diameter of 1.06 nm were applied to model the Pt NP in the 20PtCo/NC and the 6PtCo/NC samples, respectively.

The calculated free energy changes ($\Delta E_f$) for transitioning a single Pt atom from the Pt$_{55}$ NP and the extended Pt (111) surface to a PtC$_3$N site were predicted to be −0.25 and 1.69 eV, respectively (**Figure 5**a,b). Therefore, the Pt atom in the PtC$_3$N site is more thermodynamically stable than in the small Pt$_{55}$ cluster in the 6PtCo/NC sample. In contrast, it would be hard to lose Pt atoms from the extended Pt (111) surface of a large Pt NP to form a single Pt site due to the considerable positive $\Delta E_f$. Hence, as for a high loading Pt, the dominant Pt (111) surface formation prohibits the atomization process during the high-temperature annealing process. Furthermore, we found the $\Delta E_f$ for the transition of a Co site from a CoN$_4$ site to the extended L1$_2$ structured Pt$_3$Co (111) surface is −1.41 eV (Figure 5c), suggesting a thermodynamically favorable transition to alloy ordered Pt$_3$Co NPs in the 20PtCo/NC sample. Therefore, although the initially deposited Pt NPs possess similar sizes (inset in Figure 2a,b) regardless of Pt content, their separation distances of Pt NPs during annealing can eventually lead to different behaviors: alloying or atomization.
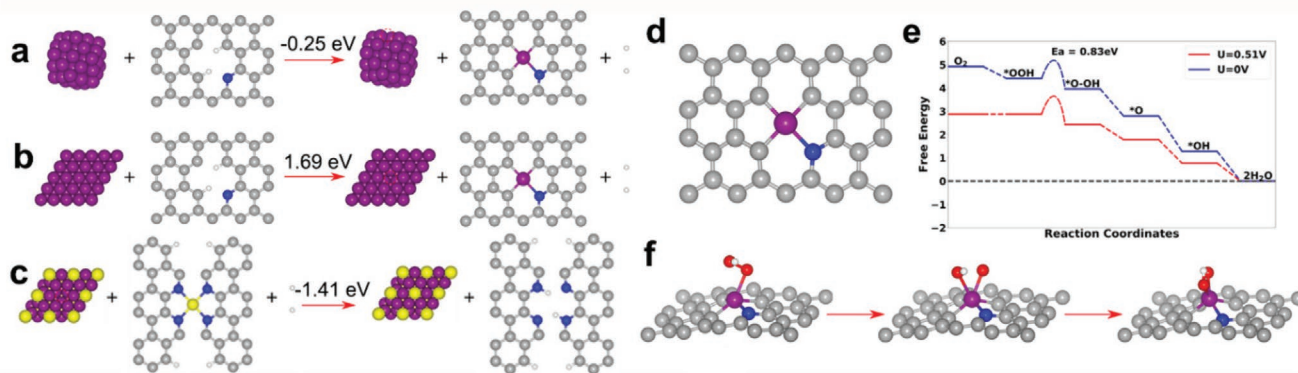
**Figure 5.** DFT calculations on the alloying versus atomization processes and ORR properties of the proposed $PtC_3N$ site. a,b) Schematics of the transition process of a Pt atom from a $Pt_{55}$ NP (a) and extended Pt(111) surface (b) to a $PtC_3N$ site. c) A Co atom from a $CoN_{2+2}$ site to the extended $Pt_3Co$ (111) surface. d) Atomic structure of a $PtC_3N$ active site. e) Calculated free energy evolution diagram for ORR through a 4e$^-$ associative pathway on the $PtC_3N$ active site under electrode potential of $U = 0.51$ V and $U = 0$ V. f) Atomistic structure of the initial state (left panel, state *OOH in (e)), transition state (middle panel) and final state (right panel, state *O—OH in (e)) for OOH dissociation reaction on the $PtC_3N$ active site. The gray, blue, purple, yellow, and white balls represent C, N, Pt, Co, and H atoms, respectively.

## 2.5. DFT and Electrochemical Studies of ORR Activity for $Pt_3Co$ and PtSA-Co Catalysts

Our DFT calculations predict a synergetic effect between Pt single metal sites and $CoN_4$ sites embedded in the NC support regarding intrinsic ORR activity. First, four possible N-coordinated active sites of $PtC_3N$, $PtC_2N_2$, $PtCN_3$, and $PtN_4$ were constructed (Figure S17, Supporting Information). The computational hydrogen electrode (CHE) method was used to predict the free energy evolution of the ORR on these sites.[59] We assumed a 4e$^-$ associative ORR pathway, where an $O_2$ molecular first adsorbs on the central Pt atom and then be protonated to form *OOH, *O, *OH, and $H_2O$ sequentially. Our calculations indicated that only the $PtC_3N$ site is thermodynamically favorable for the ORR with sufficiently high limiting potentials of 0.51 V (Figure S18, Supporting Information). Furthermore, the free energy barrier for dissociating *OOH to *O and *OH on the $PtC_3N$ site is calculated to be 0.83 eV using the climbing image nudge elastic band method (Figure 5d–f).[60] Compared to our previously reported $CoN_{2+2}$ site,[21] the $PtC_3N$ site presented a lower limiting potential (0.51 vs 0.73 V) and a higher *OOH dissociation energy barrier (0.83 vs 0.69 eV). Therefore, the isolated $PtC_3N$ site is inferior to the $CoN_{2+2}$ site for the ORR.

However, in the PtSA-Co catalyst, many neighboring dual-dots with distinct contrast can be observed in the HR-STEM images (Figure S19, Supporting Information), suggesting that the $PtC_3N$ and $CoN_4$ sites may form simultaneously during the annealing process. Our previous work showed that the $CoN_{2+2}$ (a $CoN_4$ moiety bridging over two adjacent armchair graphitic edge) site is active for the 4e$^-$ ORR.[21] To gain insight into the synergetic effect between single Pt and Co sites, we constructed a $CoN_{2+2}$–$PtC_3N$ model site with one shared N ligand (Figure S20a, Supporting Information). DFT calculations suggested that the $CoN_{2+2}$–$PtC_3N$ dual metal site exhibited enhanced ORR activity with an increased limiting potential of 0.88 V (Figure S20b, Supporting Information), higher than the isolated $PtC_3N$ (0.51 V) and the $CoN_{2+2}$ (0.73 V) sites. ORR intermediates are adsorbed at

the Co site rather than the Pt site on the proposed $CoN_{2+2}$–$PtC_3N$ active site (Table S5, Supporting Information). Furthermore, our density of state (DOS) calculations indicated that integrating the $PtC_3N$ into the $CoN_{2+2}$ site modifies the local electronic distribution near the Fermi level of Co sites (Figure S20c, Supporting Information) and leads to enhanced ORR activity. Also, the $CoN_4$ site could stabilize the neighboring $PtC_3N$ site (Figure S20d, Supporting Information). Thus, the possible modification of local electron distribution of the $PtC_3N$ site by nearby $CoN_{2+2}$ sites could enhance the ORR activity.

To experimentally compare the ORR activity of the $Pt_3Co$, Pt SAs, and Co SAs catalysts, we conducted electrochemical measurements in 0.1 M $HClO_4$ solution using the rotating disk electrode (RDE) with a typical Pt loading of 20 μg cm$^{-2}$. As displayed in **Figure 6**a, the $Pt_3Co$ and PtSA-Co catalysts presented comparable ORR activity with half-wave potentials ($E_{1/2}$) over 0.89 V versus reversible hydrogen electrode (RHE) (Table S6, Supporting Information), higher than that of a commercial Pt/Vulcan-XC-72 catalyst (0.858 V). The continuously enhanced ORR activity of the 1PtSA-Co catalyst with increased Pt loadings on the RDE (1, 4, 10, and 20 μg cm$^{-2}$) indicated that atomic single Pt sites directly contribute to the activity improvement (Figure S21a, Supporting Information). Similar ORR activity measured with the Pt/XC-72 catalyst can be achieved using the 1PtSA-Co catalyst only with a half Pt loading (10 vs 20 μg cm$^{-2}$) (Figure S21b, Supporting Information), verifying the increased intrinsic activity and Pt utilization.

The geometry and electronic structures of single metal site catalysts can be rationally tailored by changing the metal atoms, adjacent coordinative dopants and coordination numbers, enabling a flexible tunability on their electrocatalysis performance.[7,61–64] Our characterization and calculations suggest that the $PtC_3N$ site is the most suitable configuration for the atomized single Pt site on the NC support. Its synergetic effect with $CoN_{2+2}$ could significantly enhance the ORR activity. Compared with the single $CoN_4$ site catalyst (Co/NC) ($E_{1/2} = 0.810$ V), the 1PtSA-Co showed enhanced activity (Figure 6b). Moreover, the Pt SAs catalyst (1PtSA, without Co doping in NC) exhibited
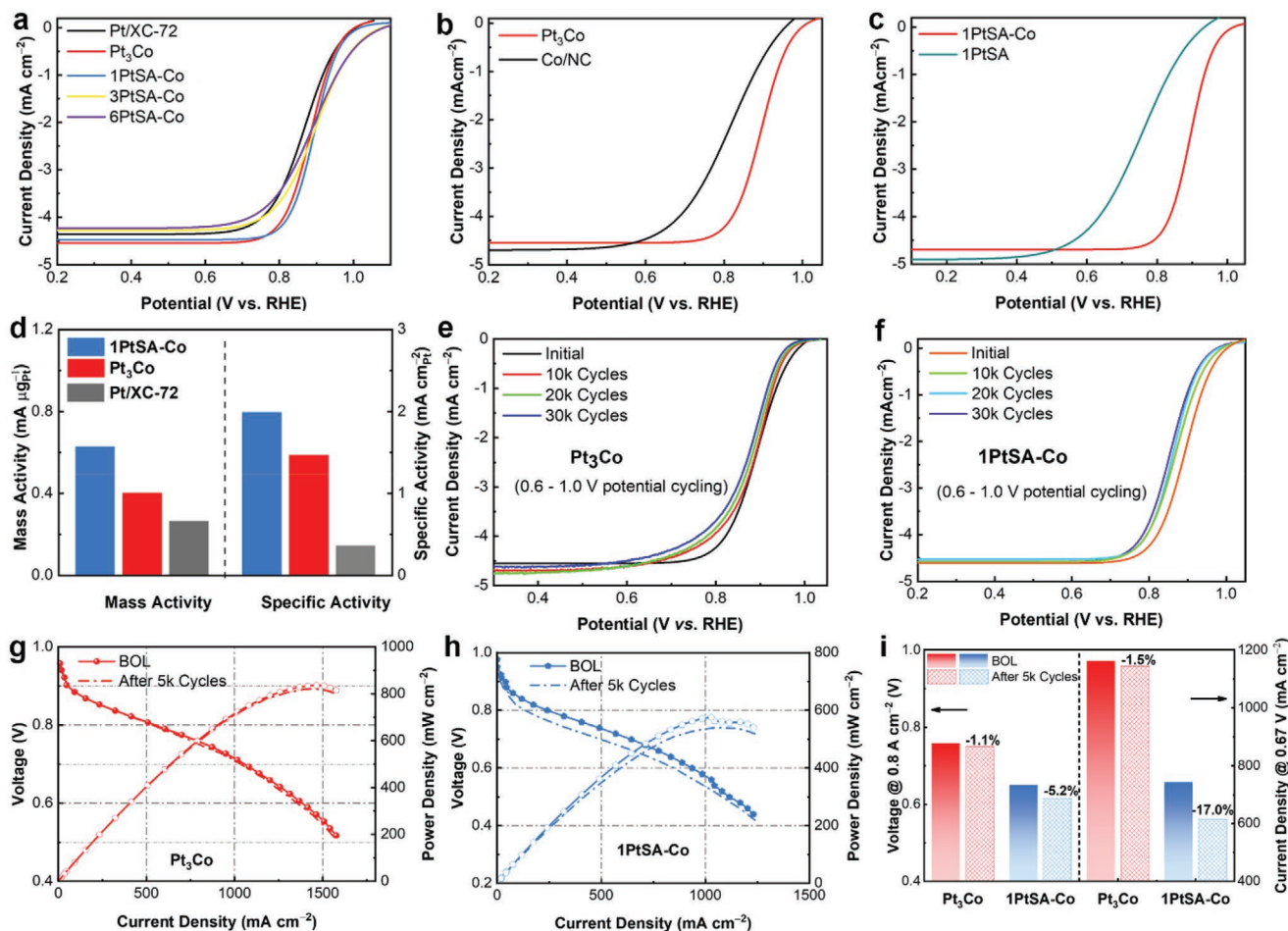
**Figure 6.** ORR performance of the $Pt_3Co$ NP and the PtSA-Co catalysts in RDE and $H_2$-air fuel cells. a–c) Steady-state polarization ORR plots for: a) $Pt_3Co$, $n$PtSA-Co ($n$ = 6 wt%, 3wt%, and 1 wt%) and Pt/XC-72; b) Co/NC and $Pt_3Co$; c) 1PtSA-Co and 1PtSA in an $O_2$-saturated 0.1 M $HClO_4$ electrolyte at room temperature with rotation rate of 1200 rpm. d) Comparison of mass and specific activities for the ORR on the $Pt_3Co$, the 1PtSA-Co, and a Pt/XC-72 catalysts. e,f) RDE potential cycling stability tests from 0.6 to1.0 V for $Pt_3Co$ (e) and 1PtSA-Co (f). g,h) MEA performance for $Pt_3Co$ (g) and 1PtSA-Co (h) before and after 5000 cycles of accelerated stress test (AST). i) Comparison of the voltage (@0.8 A $cm^{-2}$) and current density (@0.67 V) of the $Pt_3Co$ and the 1PtSA-Co catalysts before and after the AST.

a lower $E_{1/2}$ (0.750 V) than that of the Co/NC (0.810 V), which is consistent with our DFT predictions that the individual $PtC_3N$ only generates moderate activity. Thus, the combination of single Pt and Co sites in the 1PtSA-Co catalyst is superior to the individual Co-free 1PtSA and the Pt-free Co/NC catalysts (Figure 6c), further indicating the possible synergistic effect predicted by our DFT results, including i) increased limiting potential of $CoN_{2+2}$–$PtC_3N$ site, ii) modification of the local electronic distribution near the Fermi level of Co sites by $PtC_3N$ site, and iii) stabilization of $PtC_3N$ site by the $CoN_4$ site. The 1PtSA-Co catalyst exhibited higher mass activity (MA) at 0.9 $V_{iR-free}$ (630 mA $mg^{-1}_{Pt}$) than the $Pt_3Co$ (404 mA $mg^{-1}_{Pt}$) and the Pt/Vulcan-XC-72 catalysts (263 mA $mg^{-1}_{Pt}$). Besides, a comparison of specific activity based on measured electrochemical active surface areas (ECSAs) of Pt indicated that the 1PtSA catalyst is intrinsically more active (1.99 mA $cm^{-2}_{Pt}$) than $Pt_3Co$ alloy (1.47 mA $cm^{-2}_{Pt}$) and the traditional Pt NPs (0.36 mA $cm^{-2}_{Pt}$) (Figure 6d). Herein, CO stripping was employed to measure the ECSAs of 1PtSA-Co/NC and $Pt_3Co$/NC catalysts (Figure S22 and Table S7, Supporting Information).[65–67]

The accelerated stress tests (ASTs) were conducted to study catalyst stability by cycling potentials in both low (0.6–1.0 V) and high (1.0–1.5 V) ranges in 0.1 M $HClO_4$ electrolyte. It should be mentioned that the catalytic performance of PtCo alloy is closely related to the degree of ordering and surface structure.[1,3,29,30,68] Since the high degree of ordering and strong d-orbital interactions between Co and Pt in $Pt_3Co$ NPs tend to stabilize Pt and avoid Co leaching in acid solution, $Pt_3Co$ catalyst only presented an $E_{1/2}$ loss of 23 mV after 10 000 cycles in the 0.6–1.0 V range (Figure 6e; Figure S23a, Supporting Information). The $Pt_3Co$ catalyst supported by Co-doped ZIF-8-derived carbon also showed excellent stability with nearly no degradation after 5000 cycles in the 1.0–1.5 V range (Figure S23b, Supporting Information), indicating the enhanced carbon corrosion resistance and the strengthened interaction between $Pt_3Co$ NPs and the NC supports with Co and N dopants. In contrast, for the 1PtSA-Co catalyst, we observed a significant degradation with a loss of 36 mV and 50 mV in $E_{1/2}$ after 10 000 cycles from 0.6 to 1.0 V (Figure 6f) and after 5000 cycles from 1.0 to 1.5V (Figure S23c, Supporting Information), respectively.

Since both Pt SAs and Co SAs contributed to the activity, it will be desirable to decouple their accountability to the observed activity loss. Thus, we further studied the cycling stability of the Co/NC and the 1PtSA catalysts separately. After 10000 cycles in the range of 0.6–1.0 V, the $E_{1/2}$ loss of the Co/NC was only 20 mV, while the 1PtSA suffered 54 mV loss (Figure S24, Supporting Information). It suggested that the atomic Pt sites' stability is inferior to the atomic Co sites during the ORR.

The ORR performance of the Pt$_3$Co and the 1PtSA-Co catalysts were further studied in the membrane electrode assembly (MEA) under H$_2$-air conditions. As shown in Figure 6g, the Pt$_3$Co NP catalyst delivered high MEA performance (e.g., >0.5 A cm$^{-2}$ at 0.8 V and >1 A cm$^{-2}$ at 0.7 V) at an ultralow Pt cathode loading of 0.1 mg$_{Pt}$ cm$^{-2}$. A preliminary stability test by using an accelerated stress test (AST) for 5000 cycles showed insignificant potential loss (Figure 6g,i), further verified the promising stability of the Pt$_3$Co catalyst. However, the 1PtSA-Co catalyst presented a lower performance in an MEA under identical testing conditions (Figure 6h) (e.g., 0.25 A cm$^{-2}$ at 0.8 V). Compared with the Pt$_3$Co catalyst, the 1PtSA-Co catalyst suffered from noticeable performance loss after 5000 cycles of AST (Figure 6h). MEA performance of Pt$_3$Co and 1PtSA-Co before and after 5000 cycles of AST is compared in Figure 6i and Table S8, Supporting Information. Specifically, the voltage losses of the 1PtSA-Co and the Pt$_3$Co at 0.8 A cm$^{-2}$ are 5.2% and 1.1%, and their corresponding current density losses at 0.67 V are 17% and 1.5%, respectively. Thus, although the 1PtSA-Co catalyst presented significantly enhanced intrinsic activity, its stability during the ORR is insufficient and faces the grand challenge for viable applications in PEMFCs.

## 3. Conclusion

We have employed in situ advanced electron microscopy techniques and investigated the loading-dependent structural evolution of two types of critical Pt–Co binary catalysts (e.g., ordered Pt$_3$Co and single Pt/Co metal sites) at the atomic level during the essential thermal activation process. The correlations between synthesis, structures, and ORR catalytic properties for these two attractive Pt-based catalysts were studied comprehensively. As ideal carbon support, the ZIF-8-derived carbon embedded with atomically dispersed CoN$_4$ sites was identified to support Pt NPs with different loadings. At the high Pt loadings (e.g., 20%), ordered Pt$_3$Co intermetallic NPs are formed through the migration and incorporation of the Co atoms from CoN$_4$ sites into Pt NPs, accompanying the PMC and disorder–order transition processes. The initial Co structures (single Co sites or Co clusters) affect the morphology and compositional homogeneity of the synthesized PtCo NPs. On the contrary, as for the low Pt loadings (e.g., <6%), instead of alloying, Pt NPs tend to be atomized and become single Pt sites stabilized by N dopants and C defects. The nature of carbon support is critical for the atomization dynamics of Pt NPs. The atomization temperature and duration are strongly related to the initial size of deposited Pt NPs. Larger Pt NPs, higher temperature and longer duration are required for a complete atomization process. Due to the likely synergetic effect between the PtC$_3$N moiety and the surrounding CoN$_4$ site, the Pt-Co catalyst, consisting of both single Pt and Co metal sites, exhibited enhanced ORR activity than individual single Pt and Co site catalysts. However, the catalyst suffers from apparent activity degradation due to the instability of single Pt sites stabilized in carbon during the ORR. In contrast, the ordered Pt$_3$Co NPs exhibited encouraging performance and enhanced stability. The established synthesis-structure–property relationship can provide relevant knowledge for designing desirable atomic structures and compositions of Pt-based catalysts with optimal catalytic properties for crucial electrocatalysis processes.

## 4. Experimental Section

*Synthesis of the Co/NC Support*: The synthesis of the CoN$_4$-rich NC support derived from ZIF-8 precursor is followed the authors' previous work.[21] Typically, the surfactant F127 (PEO100-PPO65-PEO100, 1 g) was dissolved in methanol (25 mL), and then mixed with zinc nitrate hexahydrate (Zn(NO$_3$)$_2$·6(H$_2$O), 2.97 g, 10 mmol) and cobalt (II) nitrate hexahydrate (Co(NO$_3$)$_2$·6(H$_2$O), 0.873 g, 3 mmol)). Next, the other methanol solution (50 mL), containing 2-methylimidazole (3.2 g, 39 mmol), was subsequently injected into the above solution under stirring for 5 min at 25 °C. After heating to 60 °C for 30 min in a reflux system, pink crystal precipitates (i.e., Co-doped ZIF-8 precursor, denoted as Co/ZIF-8@F127) were collected and dried in vacuum (60 °C, 12 h).[69] The Co/ZIF-8@F127 precursors were then converted to a CoN$_4$-site-rich carbon (i.e., Co/NC) at 900 °C under N$_2$ atmosphere for three hours followed by a leaching treatment with 2 M HCl at 60 °C for 5 h. The NC (without Co doping) support was synthesized by the same method without adding Co(NO$_3$)$_2$·6(H$_2$O) to the precursors.

*Preparation of nPtCo/NC*: The *n*PtCo/NC was obtained by using an ethylene glycol (EG) reduction method. Typically, the Co/NC supports were sonicated in EG solution. Then, a certain amount of chloroplatinic acid (CPA) solution (in EG) was added to the slurry and stirred for 30 min. After being heated up to 135 °C and refluxed for three hours under magnetic stirring, the catalysts were washed with deionized water and dried at 80 °C in a vacuum oven to obtain *n*PtCo/NC (*n* is the Pt loading against the Co/NC support). Synthesis of NC (without Co doping) supported PtNPs (Pt/NC) was synthesized by the same method by using the NC as the supports.

*In Situ Electron Microscopy Heating Experiments and Characterization*: In situ heating experiments inside TEM were performed with a heating stage of DENS Solutions. The in situ TEM and EDX mappings were performed on a high-resolution analytical S/TEM (FEI Talos F200X), equipped with a four-quadrant 0.9-sr EDX spectrometer. Atomic-resolution HAADF-STEM images were acquired with HD2700C STEM (Hitachi) equipped with a probe aberration corrector. XPS spectroscopy experiments were carried out in an ultrahigh vacuum system equipped a hemispherical electron energy analyzer (SPECS, PHOIBOS 100) and a twin-anode X-ray source (SPECS, XR50). The XANES and EXAFS measurements of Co K-edge and Pt L$_3$-edge were carried out at the beamline 7-BM (QAS) of the National Synchrotron Light Source II (NSLS-II). The Co foil and Pt foil were used for the energy calibration, and all samples were ex situ measured under transmission mode at RT. Data processing of the XANES and EXAFS spectra were performed using the IFEFFIT package. The Fourier transform EXAFS fittings were performed with the back-scattering amplitude and phase shift obtained from the corresponding paths (Pt–C, Pt–N, Pt–Pt, and Pt–Co) in the PtC$_{4-x}$N$_x$ and Pt–Co dual-site models. Wavelet transform EXAFS contours were plotted by the EvAX code.

*Electrochemical Measurements*: The electrochemical measurements were carried out by using an electrochemical workstation (CHI760b) coupled with a rotating-ring disk electrode (RRDE, Pine, AFMSRCE 3005) in a 0.1 M HClO$_4$ electrolyte by using a three-electrode cell (see Supporting Information). The ECSAs of these Pt-based catalysts were determined by using CO stripping (see Supporting Information).

Experimental details about fuel cell tests were provided in the Supporting Information.

*Theoretical Calculations*: The first-principles DFT calculations with plane-wave basis set were carried out using the Vienna Ab initio Simulation Package (VASP). The details can be found in the Supporting Information.

## Supporting Information

Supporting Information is available from the Wiley Online Library or from the author.

## Acknowledgements

## Conflict of Interest

The authors declare no conflict of interest.

## Data Availability Statement

Research data are not shared.

## Keywords

[1] X. X. Wang, S. Hwang, Y. T. Pan, K. Chen, Y. He, S. Karakalos, H. Zhang, J. S. Spendelow, D. Su, G. Wu, *Nano Lett.* **2018**, *18*, 4163.
[2] L. Chong, J. Wen, J. Kubal, F. G. Sen, J. Zou, J. Greeley, M. Chan, H. Barkholtz, W. Ding, D.-J. Liu, *Science* **2018**, *362*, 1276.
[3] D. Wang, H. L. Xin, R. Hovden, H. Wang, Y. Yu, D. A. Muller, F. J. DiSalvo, H. D. Abruna, *Nat. Mater.* **2013**, *12*, 81.
[4] X. X. Wang, M. T. Swihart, G. Wu, *Nat. Catal.* **2019**, *2*, 578.
[5] N. Du, C. Wang, R. Long, Y. Xiong, *Nano Res.* **2017**, *10*, 3228.
[6] J. Li, S. Sharma, X. Liu, Y.-T. Pan, J. S. Spendelow, M. Chi, Y. Jia, P. Zhang, D. A. Cullen, Z. Xi, H. Lin, Z. Yin, B. Shen, M. Muzzio, C. Yu, Y. S. Kim, A. A. Peterson, K. L. More, H. Zhu, S. Sun, *Joule* **2019**, *3*, 124.
[7] C. Tang, Y. Jiao, B. Shi, J. N. Liu, Z. Xie, X. Chen, Q. Zhang, S. Z. Qiao, *Angew. Chem., Int. Ed.* **2020**, *59*, 9171.
[8] Z. Zhang, Y. Chen, L. Zhou, C. Chen, Z. Han, B. Zhang, Q. Wu, L. Yang, L. Du, Y. Bu, P. Wang, X. Wang, H. Yang, Z. Hu, *Nat. Commun.* **2019**, *10*, 1657.
[9] J. Li, H. Zhang, W. Samarakoon, W. Shan, D. A. Cullen, S. Karakalos, M. Chen, D. Gu, K. L. More, G. Wang, Z. Feng, Z. Wang, G. Wu, *Angew. Chem., Int. Ed.* **2019**, *58*, 18971.
[10] W. Chen, J. Pei, C. T. He, J. Wan, H. Ren, Y. Wang, J. Dong, K. Wu, W. C. Cheong, J. Mao, X. Zheng, W. Yan, Z. Zhuang, C. Chen, Q. Peng, D. Wang, Y. Li, *Adv. Mater.* **2018**, *30*, 1800396.
[11] N. Cheng, S. Stambula, D. Wang, M. N. Banis, J. Liu, A. Riese, B. Xiao, R. Li, T. K. Sham, L. M. Liu, G. A. Botton, X. Sun, *Nat. Commun.* **2016**, *7*, 13638.
[12] S. Wei, A. Li, J. C. Liu, Z. Li, W. Chen, Y. Gong, Q. Zhang, W. C. Cheong, Y. Wang, L. Zheng, H. Xiao, C. Chen, D. Wang, Q. Peng, L. Gu, X. Han, J. Li, Y. Li, *Nat. Nanotechnol.* **2018**, *13*, 856.
[13] J. Yang, Z. Qiu, C. Zhao, W. Wei, W. Chen, Z. Li, Y. Qu, J. Dong, J. Luo, Z. Li, Y. Wu, *Angew. Chem., Int. Ed.* **2018**, *57*, 14095.
[14] Y. Qu, B. Chen, Z. Li, X. Duan, L. Wang, Y. Lin, T. Yuan, F. Zhou, Y. Hu, Z. Yang, C. Zhao, J. Wang, C. Zhao, Y. Hu, G. Wu, Q. Zhang, Q. Xu, B. Liu, P. Gao, R. You, W. Huang, L. Zheng, L. Gu, Y. Wu, Y. Li, *J. Am. Chem. Soc.* **2019**, *141*, 4505.
[15] Y. Li, H. Wang, C. Priest, S. Li, P. Xu, G. Wu, *Adv. Mater.* **2021**, *33*, 2000381.
[16] D. Y. Chung, S. W. Jun, G. Yoon, S. G. Kwon, D. Y. Shin, P. Seo, J. M. Yoo, H. Shin, Y. H. Chung, H. Kim, B. S. Mun, K. S. Lee, N. S. Lee, S. J. Yoo, D. H. Lim, K. Kang, Y. E. Sung, T. Hyeon, *J. Am. Chem. Soc.* **2015**, *137*, 15478.
[17] Y. Yao, Z. Huang, P. Xie, L. Wu, L. Ma, T. Li, Z. Pang, M. Jiao, Z. Liang, J. Gao, Y. He, D. J. Kline, M. R. Zachariah, C. Wang, J. Lu, T. Wu, T. Li, C. Wang, R. Shahbazian-Yassar, L. Hu, *Nat. Nanotechnol.* **2019**, *14*, 851.
[18] H. Hayashi, A. P. Cote, H. Furukawa, M. O'Keeffe, O. M. Yaghi, *Nat. Mater.* **2007**, *6*, 501.
[19] H. Zhang, J. Li, Q. Tan, L. Lu, Z. Wang, G. Wu, *Chem. - Eur. J.* **2018**, *24*, 18137.
[20] Q. Ren, H. Wang, X. F. Lu, Y. X. Tong, G. R. Li, *Adv. Sci.* **2018**, *5*, 1700515.
[21] Y. He, S. Hwang, D. A. Cullen, M. A. Uddin, L. Langhorst, B. Li, S. Karakalos, A. J. Kropf, E. C. Wegener, J. Sokolowski, M. Chen, D. Myers, D. Su, K. L. More, G. Wang, S. Litster, G. Wu, *Energy Environ. Sci.* **2019**, *12*, 250.
[22] J. Li, M. Chen, D. A. Cullen, S. Hwang, M. Wang, B. Li, K. Liu, S. Karakalos, M. Lucero, H. Zhang, C. Lei, H. Xu, G. E. Sterbinsky, Z. Feng, D. Su, K. L. More, G. Wang, Z. Wang, G. Wu, *Nat. Catal.* **2018**, *1*, 935.
[23] X. Fang, Q. Shang, Y. Wang, L. Jiao, T. Yao, Y. Li, Q. Zhang, Y. Luo, H. L. Jiang, *Adv. Mater.* **2018**, *30*, 1705112.
[24] H. Zhang, S. Hwang, M. Wang, Z. Feng, S. Karakalos, L. Luo, Z. Qiao, X. Xie, C. Wang, D. Su, Y. Shao, G. Wu, *J. Am. Chem. Soc.* **2017**, *139*, 14143.
[25] H. Zhang, H. T. Chung, D. A. Cullen, S. Wagner, U. I. Kramm, K. L. More, P. Zelenay, G. Wu, *Energy Environ. Sci.* **2019**, *12*, 2548.
[26] Q. Shi, Y. He, X. Bai, M. Wang, D. A. Cullen, M. Lucero, X. Zhao, K. L. More, H. Zhou, Z. Feng, Y. Liu, G. Wu, *Energy Environ. Sci.* **2020**, *13*, 3544.
[27] T. S. Ahmadi, Z. L. Wang, T. C. Green, A. Henglein, M. A. EI-Sayed, *Science* **1996**, *272*, 1924.
[28] J. Wu, A. Gross, H. Yang, *Nano Lett.* **2011**, *11*, 798.
[29] S. Dai, Y. You, S. Zhang, W. Cai, M. Xu, L. Xie, R. Wu, G. W. Graham, X. Pan, *Nat. Commun.* **2017**, *8*, 204.
[30] Y. Xiong, Y. Yang, H. Joress, E. Padgett, U. Gupta, V. Yarlagadda, D. N. Agyeman-Budu, X. Huang, T. E. Moylan, R. Zeng, A. Kongkanand, F. A. Escobedo, J. D. Brock, F. J. DiSalvo, D. A. Muller, H. D. Abruña, *Proc. Natl. Acad. Sci. U. S. A.* **2019**, *116*, 1974.
[31] H. L. Xin, S. Alayoglu, R. Tao, A. Genc, C. M. Wang, L. Kovarik, E. A. Stach, L. W. Wang, M. Salmeron, G. A. Somorjai, H. Zheng, *Nano Lett.* **2014**, *14*, 3203.

**ADVANCED
SCIENCE NEWS**

www.advancedsciencenews.com

**ADVANCED
MATERIALS**

www.advmat.de

[32] Z. Qiao, C. Wang, C. Li, Y. Zeng, S. Hwang, B. Li, S. Karakalos, J. Park, A. J. Kropf, E. C. Wegener, Q. Gong, H. Xu, G. Wang, D. J. Myers, J. Xie, J. S. Spendelow, G. Wu, *Energy Environ. Sci.* **2021**, *14*, 4948.

[33] H. Fei, J. Dong, Y. Feng, C. S. Allen, C. Wan, B. Volosskiy, M. Li, Z. Zhao, Y. Wang, H. Sun, P. An, W. Chen, Z. Guo, C. Lee, D. Chen, I. Shakir, M. Liu, T. Hu, Y. Li, A. I. Kirkland, X. Duan, Y. Huang, *Nat. Catal.* **2018**, *1*, 63.

[34] Y. He, Q. Shi, W. Shan, X. Li, A. J. Kropf, E. C. Wegener, J. Wright, S. Karakalos, D. Su, D. A. Cullen, G. Wang, D. J. Myers, G. Wu, *Angew. Chem., Int. Ed.* **2021**, *60*, 9516.

[35] Y. He, H. Guo, S. Hwang, X. Yang, Z. He, J. Braaten, S. Karakalos, W. Shan, M. Wang, H. Zhou, Z. Feng, K. L. More, G. Wang, D. Su, D. A. Cullen, L. Fei, S. Litster, G. Wu, *Adv. Mater.* **2020**, *32*, 2003577.

[36] Y. He, S. Liu, C. Priest, Q. Shi, G. Wu, *Chem. Soc. Rev.* **2020**, *49*, 3484.

[37] Y. Zhu, J. Sokolowski, X. Song, Y. He, Y. Mei, G. Wu, *Adv. Energy Mater.* **2020**, *10*, 1902844.

[38] D. Alloyeau, C. Ricolleau, C. Mottet, T. Oikawa, C. Langlois, Y. L. Bouar, N. Braidy, A. Loiseau, *Nat. Mater.* **2009**, *8*, 940.

[39] M. Chi, C. Wang, Y. Lei, G. Wang, D. Li, K. L. More, A. Lupini, L. F. Allard, N. M. Markovic, V. R. Stamenkovic, *Nat. Commun.* **2015**, *6*, 8925.

[40] M. Delalande, M. J. F. Guinel, L. F. Allard, A. Delattre, R. L. Bris, Y. Samson, P. Bayle-Guillemaud, P. Reiss, *J. Phys. Chem. C* **2012**, *116*, 6866.

[41] T. W. Hansen, A. T. Delariva, S. R. Challa, A. K. Datye, *Acc. Chem. Res.* **2013**, *46*, 1720.

[42] S. B. Simonsen, I. Chorkendorff, S. Dahl, M. Skoglundh, J. Sehested, S. Helveg, *J. Am. Chem. Soc.* **2010**, *132*, 7968.

[43] S. R. Challa, A. T. Delariva, T. W. Hansen, S. Helveg, J. Sehested, P. L. Hansen, F. Garzon, A. K. Datye, *J. Am. Chem. Soc.* **2011**, *133*, 20672.

[44] D. Alloyeau, G. Prevot, Y. L. Bouar, T. Oikawa, C. Langlois, A. Loiseau, C. Ricolleau, *Phys. Rev. Lett.* **2010**, *105*, 255901.

[45] L. Fei, S. Lei, W. B. Zhang, W. Lu, Z. Lin, C. H. Lam, Y. Chai, Y. Wang, *Nat. Commun.* **2016**, *7*, 12206.

[46] W. Hou, A. Azizimanesh, A. Sewaket, T. Pena, C. Watson, M. Liu, H. Askari, S. M. Wu, *Nat. Nanotechnol.* **2019**, *14*, 668.

[47] M. A. Asoro, D. Kovar, P. J. Ferreira, *ACS Nano* **2013**, *7*, 7844.

[48] G. Prevot, N. T. Nguyen, D. Alloyeau, C. Ricolleau, J. Nelayah, *ACS Nano* **2016**, *10*, 4127.

[49] J. E. S. van der Hoeven, T. A. J. Welling, T. A. G. Silva, J. E. van den Reijen, C. L. Fontaine, X. Carrier, C. Louis, A. van Blaaderen, P. E. de Jongh, *ACS Nano* **2018**, *12*, 8467.

[50] Z. Qiao, S. Hwang, X. Li, C. Wang, W. Samarakoon, S. Karakalos, D. Li, M. Chen, Y. He, M. Wang, Z. Liu, G. Wang, H. Zhou, Z. Feng, D. Su, J. S. Spendelow, G. Wu, *Energy Environ. Sci.* **2019**, *12*, 2830.

[51] S. C. Parker, C. T. Campbell, *Phys. Rev. B* **2007**, *75*, 035430.

[52] J. Liu, M. Jiao, L. Lu, H. M. Barkholtz, Y. Li, Y. Wang, L. Jiang, Z. Wu, D. J. Liu, L. Zhuang, C. Ma, J. Zeng, B. Zhang, D. Su, P. Song, W. Xing, W. Xu, Y. Wang, Z. Jiang, G. Sun, *Nat. Commun.* **2017**, *8*, 15938.

[53] X. Li, W. Bi, L. Zhang, S. Tao, W. Chu, Q. Zhang, Y. Luo, C. Wu, Y. Xie, *Adv. Mater.* **2016**, *28*, 2427.

[54] P. Wynblatt, N. A. Gjostein, *Prog. Solid State Chem.* **1975**, *9*, 21.

[55] P. J. F. Harris, *Int. Mater. Rev.* **1995**, *40*, 97.

[56] W.-C. Yang, M. Zeman, H. Ade, R. J. Nemanich, *Phys. Rev. Lett.* **2003**, *90*, 136102.

[57] R. Ouyang, J. X. Liu, W.-X. Li, *J. Am. Chem. Soc.* **2013**, *135*, 1760.

[58] W. Yuan, D. Zhang, Y. Ou, K. Fang, B. Zhu, H. Yang, T. W. Hansen, J. B. Wagner, Z. Zhang, Y. Gao, Y. Wang, *Angew. Chem., Int. Ed.* **2018**, *57*, 16827.

[59] J. K. Norskov, J. Rossmeisl, A. Logadottir, L. Lindqvist, J. R. Kitchin, T. Bligaard, H. Jonsson, *J. Phys. Chem. B* **2004**, *108*, 17886.

[60] G. Henkelman, B. P. Uberuaga, H. Jonsson, *J. Chem. Phys.* **2000**, *113*, 9901.

[61] J. Yang, W. Li, D. Wang, Y. Li, *Adv. Mater.* **2020**, *32*, 2003300.

[62] C. Fan, X. Jiang, J. Chen, X. Wang, S. Qian, C. Zhao, L. Ding, D. Sun, Y. Tang, *Small Struct.* **2021**, *2*, 2000017.

[63] J. Yang, W. Li, D. Wang, Y. Li, *Small Struct.* **2021**, *2*, 2000051.

[64] X. Yang, M. Wang, M. J. Zachman, H. Zhou, Y. He, S. Liu, H.-Y. Zang, Z. Feng, G. Wu, *Small Sci.* 2100046. https://doi.org/10.1002/smsc.202100046.

[65] D. F. van der Vliet, C. Wang, D. Li, A. P. Paulikas, J. Greeley, R. B. Rankin, D. Strmcnik, D. Tripkovic, N. M. Markovic, V. R. Stamenkovic, *Angew. Chem., Int. Ed.* **2012**, *51*, 3139.

[66] Y. Xiong, Y. Yang, F. J. DiSalvo, H. D. Abruña, *ACS Nano* **2020**, *14*, 13069.

[67] B. Y. Xia, H. B. Wu, N. Li, Y. Yan, X. W. Lou, X. Wang, *Angew. Chem., Int. Ed.* **2015**, *54*, 3797.

[68] X. Li, J. Zhao, D. Su, *Small Struct.* **2021**, *2*, 2100011.

[69] Y. Xiang, S. Gao, R.-G. Xu, W. Wu, Y. Leng, *Nano Energy* **2019**, *58*, 202.